Chemical Engineering Journal 532 (2026) 174240

Contents lists available at ScienceDirect

Chemical Engineering Journal

journal homepage: www.elsevier.com/locate/cej

Exploring water transport in membrane electrode assemblies for CO_2 electrolyzers via multiphysics modeling

Nasim Heydari [a,*,1], Niels J. Böcker [a,1], David A. Vermaas [a], Johan T. Padding [b,*], J. Ruud van Ommen [a]

[a] Department of Chemical Engineering, Delft University of Technology, Delft, the Netherlands
[b] Department of Process and Energy, Delft University of Technology, Delft, the Netherlands

ARTICLE INFO

Keywords:
Membrane electrode assembly
Anion exchange membrane
Multiphysics
Water balance
Homogeneous buffer reactions

ABSTRACT

The long-term operation of CO_2 electrolyzers using membrane electrode assemblies (MEAs) is limited by challenges related to water management. However, the water balance in CO_2 electrolyzer cells still has not been fully understood, and conflicting observations have been reported in the literature. In this study, a one-dimensional non-isothermal multiphysics model of an exchange MEA CO_2 electrolyzer with a Tokuyama A201 anion exchange membrane is developed to investigate the role of different physical and chemical phenomena on the water balance. The relative contributions of these processes vary with current density and membrane transport properties, which shift the dominant water transport mechanism in the cell. Our results highlight the significant contribution of homogeneous reactions, particularly OH^-, to the water balance across the membrane. At low currents ($i < 130$ mA cm^{-2}), homogeneous buffer reactions dominate the water balance and result in net water production near the catalyst layer. At higher currents ($i > 130$ mA cm^{-2}), the flux is governed by electro-osmotic drag and a temperature gradient over the cathode gas diffusion electrode (GDE) with their relative contributions depending on membrane properties. Homogeneous buffering can re-emerge as the dominant mechanism at high currents if the hydroxide ion concentration in the membrane increases, for example under CO_2-limited cathode conditions, allowing hydroxide ions to react with depleted bicarbonate near the anode.

1. Introduction

CO_2 electrolysis offers a promising pathway for storing excess renewable energy in the form of chemical bonds, providing both energy storage and carbon mitigation benefits [1–3]. As of February 2025, the atmospheric CO_2 concentration has reached approximately 427 ppm, which shows an increase of 50% over the past two centuries [4]. This highlights the urgent need to reduce CO_2 emissions by capturing and converting anthropogenic CO_2 emissions. By decoupling the chemical industry from fossil fuels, CO_2 electrolysis supports the transition toward more sustainable processes. At the same time, it can contribute to emission reductions in other carbon-intensive sectors, such as energy, cement, and steel production [5].

Techno-economic analyses show that current densities above 200 mA cm^{-2}, with high selectivity (>80%) and operational stability over several months at low applied potentials (<3 V), are essential for industrial application [6,7]. MEAs have become a preferred design, by minimizing ohmic losses and mitigating issues such as electrode flooding and salt precipitation [3]. Nevertheless, sustaining high current density operation over extended periods remains challenging, with premature cell failure often attributed to water flooding and salt accumulation in the electrodes [7].

While continuum modeling of CO_2 electrolysis cells has provided insight into overall cell performance by capturing ion transport, water transport, and heat transfer, there remains a lack of focused studies on water management. In particular, the complex interplay between various transport mechanisms and their influence on water flux within the cell is not yet well understood. This coupling is critical, as it underlies key stability challenges such as electrode flooding and membrane dry-out, both of which severely affect the durability and efficiency of MEAs.

Effective design of CO_2 electrolysis cells requires a thorough understanding of water management. However, the literature reveals a limited -and sometimes contradictory- understanding of the underlying

* Corresponding authors.
E-mail addresses: n.heydari@tudelft.nl (N. Heydari), j.t.padding@tudelft.nl (J.T. Padding).
[1] These authors contributed equally to this work.

https://doi.org/10.1016/j.cej.2026.174240
Received 7 October 2025; Received in revised form 16 January 2026; Accepted 15 February 2026
Available online 19 February 2026

transport phenomena [8]. Moreover, most modeling studies prioritize overall cell performance metrics, while water transport is often treated as a secondary consideration [3,9].

This paper investigates the coupled transport mechanisms of water, ions, and heat in a CO_2 reduction MEA using continuum modeling. A one-dimensional multiphysics cell model is developed and validated against experimental polarization curves and Faradaic efficiency (FE) data. The model is used to examine how different transport mechanisms interact across a range of current densities, identifying the dominant mechanisms under varying operating conditions. The impact of anion exchange membrane (AEM) properties, specifically transport parameters and thickness, is explored. This study provides guidelines on how relative contributions and interactions of different physical and chemical phenomena in the cell affect the water balance, thus affecting the cell performance and stability.

2. Theory and model

A 1D continuum model was developed in COMSOL Multiphysics 6.2 (Fig. 1). The model represents an exchange-MEA cell, where the cathode catalyst layer is composed of silver (Ag) particles to convert CO_2 to syngas. The membrane is an AEM with a thickness of 50 μm, which is a typical value for Tokuyama A201 in MEA cells. The effect of membrane thickness is investigated in the final section of results and discussion, where we also study 20 and 80 μm thick AEM. A 10 nm ionomer coating is assumed on the catalyst particles within the catalyst layer, which has a total thickness of 5 μm. The adjacent diffusion medium (DM) has a thickness of 325 μm [10].

The anode is supplied with a fast-circulating 0.5 M $KHCO_3$ aqueous electrolyte, while the cathode GDE is exposed to fully humidified CO_2 (100% RH) from the gas channel (CH) of the flow plates.

The membrane is modeled as a homogeneous solid electrolyte with a fixed positive charge density. The CL is modeled as a porous medium containing gas, liquid, and ionomer phases. Ion transport in the liquid phase within the CL is neglected, under the assumption that the ionomer provides sufficient ionic conductivity toward the Ag particles [11]. The anode CL is modeled as a boundary. The model is validated against experimental polarization curves and Faradaic efficiency (FE) data (Fig. S2a and b) reported by Hansen et al. [12].

2.1. Governing equations

The charge transport in the solid fractions of the DM and the CL by electrons is governed by charge conservation as

$$\nabla.\mathbf{i}_S = -\nabla.\mathbf{i}_L = -\sum_k a_{v,k} i_k \tag{1}$$

where $\mathbf{i}_S$ is the electronic current density, $\mathbf{i}_L$ is the electrolyte current density, i_k is the local current density for electrochemical reaction k taking place at the catalytic particle/ionomer binder interface in CL and $a_{v,k}$ is the specific surface area. For the CO evolution reaction (COER), a correction is applied to the intrinsic specific surface area to account for the blocked access to active sites in the CL, $a_{v,COER} = (1 - S_{CL})a_{v,CL}$ [3].

The right-hand side of Eq. (1) is zero for AEM and DM. The solid phase electronic current density is modeled with Ohm's law

$$\mathbf{i}_S = -\sigma_{S,d}^{eff} \nabla \phi_S \tag{2}$$

where $\sigma_{S,d}^{eff}$ is the effective conductivity of the solid phase in domain d, determined using the Bruggeman relation $\left(\sigma_{S,d}^{eff} = \varepsilon_{S,d}^{0\ 1.5} \sigma_{S,d}\right)$ and ϕ_S is the electronic potential in the solid. The electrolyte current density is calculated from the ionic species fluxes

$$\mathbf{i}_L = F\sum_j z_j \mathbf{N}_j \tag{3}$$

where F is Faraday's constant, z_j is the charge, and $\mathbf{N}_j$ is the molar flux of species j. Here we note already that the electronic potential in the electrolyte ϕ_L is determined by solving explicit equations for the molar fluxes through Eqs. (4) and (38).

The governing equation for the mass transfer of the dissolved species and water in the electrolyte phase, is given by the molar conservation of species

$$\nabla.\mathbf{N}_j = R_{CT,j} + R_{B,j} + R_{PT,j} \tag{4}$$

where $R_{CT,j}$ is the volumetric source term due to charge transfer reactions, $R_{B,j}$ is the volumetric source term due to homogeneous buffer reactions, and $R_{PT,j}$ is the volumetric source term due to phase transfer. The gaseous species H_2 and CO are neglected in the electrolyte phase due to their low solubility.

For the gas phase species i (CO_2, H_2O, CO, H_2) the governing mass conservation equation is

$$\nabla.\mathbf{j}_i + \rho_G(\mathbf{u}_G.\nabla)\omega_i = R_{CT,i} + R_{PT,i} \tag{5}$$

where $\mathbf{j}_i$ is the diffusive mass flux of species i, ρ_G is the total gas phase density, $\mathbf{u}_G$ is the mass-averaged gas phase velocity, ω_i is the mass fraction, $R_{CT,i}$ volumetric source term due to charge transfer reactions, and $R_{PT,i}$ is the volumetric source term due to phase transfer of species i.

For porous media, i.e., CL and DM, the general momentum balance of each phase can be simplified to Darcy's Law

$$\mathbf{u}_p = -\frac{k_{d,p}^{eff}}{\mu_p}\nabla p_p \tag{6}$$

where $\mathbf{u}_p$ is the mass-average velocity, $k_{d,p}^{eff}$ is the effective permeability, μ_p is the dynamic viscosity, and p_p is the pressure of phase p. The mass balances for the gas and liquid phase are given as

$$\nabla.(\rho_p\,\mathbf{u}_p) = \Phi_p \tag{7}$$

where ρ_p is the density, and Φ_p is the volumetric mass source term, calculated by Eqs. (74) and (75).

2.2. Multiphase flow in porous media

The capillary pressure in porous domains is defined as

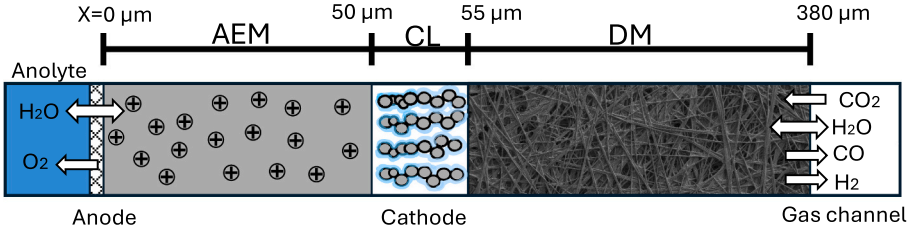

Fig. 1. Schematic view of the exchange-MEA cell and the representative domain (not to scale). The domain contains the anode as the interface on the left (at 0 μm), the anion exchange membrane (AEM), catalyst layer (CL), diffusion medium (DM), and finally the gas channel (CH) as the interface on the right.

$$p_{cap} = p_L - p_G \tag{8}$$

The liquid saturations of the porous domains are determined by interpolating experimental water saturation data from Zenyuk et al. [13] (Fig. S1). The effective permeability of the porous media is dependent on saturation through the relative permeability

$$k_{d,P}^{eff} = k_d^{sat} k_{d,P}^r \tag{9}$$

where k_d^{sat} is the saturated permeability of domain d, and $k_{d,P}^r$ is the relative permeability for phase p. The relative permeability is calculated for the liquid and gaseous phases according to

$$k_{d,L}^r = (S_d)^3 \tag{10}$$

$$k_{d,G}^r = (1 - S_d)^3 \tag{11}$$

where the gas saturation of the pores is $(1 - S_d)$, and a cubic dependence is assumed for the relative permeability on water saturation [14]. Furthermore, the volume fraction of different phases in the porous domains is defined as

$$\varepsilon_{S,d} = 1 - \varepsilon_d^0 \tag{12}$$

$$\varepsilon_{I,d} = \varepsilon_d^0 f_{I,d} \tag{13}$$

$$\varepsilon_{L,d} = \varepsilon_d^0 \left(1 - f_{I,d}\right) S_d \tag{14}$$

$$\varepsilon_{G,d} = \varepsilon_d^0 \left(1 - f_{I,d}\right) (1 - S_d) \tag{15}$$

where ε_d^0 is the intrinsic porosity of domain d and $f_{I,d}$ is the volume fraction of ionomer within the pore space. Furthermore, other effective properties in the porous domains are corrected for the porosity and the tortuosity following Bruggeman's equation

$$X_{d,P}^{eff} = \left(\frac{\varepsilon}{\tau} X^{bulk}\right)_{d,P} = \left(\varepsilon^{3/2} X^{bulk}\right)_{d,P} \tag{16}$$

where $X_{d,P}^{eff}$ is the effective property in domain d for phase p.

2.3. Electrochemistry

Charge transfer reactions occur at the anode and at the cathode. At the anode interface the oxygen evolution reaction (OER) occurs according to both acidic and alkaline reactions

$$2H_2O \rightarrow O_2 + 4H^+ + 4e^- \tag{17}$$

$$4OH^- \rightarrow O_2 + 2H_2O + 4e^- \tag{18}$$

While at the porous cathode catalyst/ionomer interface the hydrogen evolution reaction (HER) and CO evolution reaction (COER) occur. The HER proceeds through both the acidic and alkaline reactions

$$2H^+ + 2e^- \rightarrow H_2 \tag{19}$$

$$2H_2O + 2e^- \rightarrow H_2 + 2OH^- \tag{20}$$

The COER proceeds via

$$CO_2 + H_2O + 2e^- \rightarrow CO + 2OH^- \tag{21}$$

The kinetics for these reactions are modeled with the Tafel equation, including a concentration or water activity dependent term for the cathode (COER, HER in base, HER in acid) and anode (OER in base, OER in acid), respectively.

$$i_{COER} = -i_{o,COER} \left(\frac{c_{CO2}}{1[M]}\right)^{1.5} a_w \exp\left(-\frac{\alpha_{c,COER} F}{RT} \eta_{COER}\right) \tag{22}$$

$$i_{HER,base} = -i_{o,HER,base} {a_w}^2 \exp\left(-\frac{\alpha_{c,HER} F}{RT} \eta_{HER}\right) \tag{23}$$

$$i_{HER,acid} = -i_{o,HER} \left(\frac{c_{H^+}}{1[M]}\right) a_w \exp\left(-\frac{\alpha_{c,HER} F}{RT} \eta_{HER}\right) \tag{24}$$

$$i_{OER,base} = -i_{o,OER} \left(\frac{c_{OH^-}}{1[M]}\right) \exp\left(-\frac{\alpha_{a,OER} F}{RT} \eta_{OER}\right) \tag{25}$$

$$i_{OER,acid} = -i_{o,OER} \exp\left(-\frac{\alpha_{a,OER} F}{RT} \eta_{OER}\right) \tag{26}$$

where for charge transfer reaction k, $i_{o,k}$ is the exchange current density, $\alpha_{c,k}$ and $\alpha_{a,k}$ are the cathodic and anodic transfer coefficients, and η_k is the reaction overpotential. An expression for the water activity a_w will be introduced later.

The exchange current density is modeled with an Arrhenius expression

$$i_{o,k} = A_k \exp\left(-\frac{E_{a,k}}{RT}\right) \tag{27}$$

where A_k is the pre-exponential factor, and $E_{a,k}$ the apparent activation energy. The reaction overpotential is defined as

$$\eta_k = \phi_S - \phi_L - E_{eq,k} \tag{28}$$

where ϕ_L is the electrolyte potential, and $E_{eq,k}$ is the reaction equilibrium potential calculated with a simplified Nernst equation

$$E_{eq,k} = E_{eq,k}^0 - \frac{2.303RT}{F} \mathrm{pH} \tag{29}$$

where $E_{eq,k}^0$ is the standard reduction potential defined at pH = 0.

The electrochemical reactions contribute to the source terms $R_{CT,j}$ and $R_{CT,i}$ for the dissolved species (CO_2, H^+, OH^-, H_2O) and for the gaseous species (CO and H_2)

$$R_{CT,j} = -\sum_k \frac{\nu_{j,k} a_{v,k} i_k}{n_k F} \tag{30}$$

where $\nu_{j,k}$ is the stoichiometric coefficient of species j in reaction k, and n_k the number of electrons involved in the reaction. The specific surface area is corrected to $a_{v,COER} = (1 - S_{CL}) a_{v,CL}$ for COER [3].

2.4. Homogeneous reaction chemistry

In the electrolyte phase, the membrane and the ionomer, the following homogeneous buffer reactions occur

$$H_2O \xleftrightarrow{k_1, k_{-1}} H^+ + OH^- \tag{31}$$

$$CO_2 + H_2O \xleftrightarrow{k_2, k_{-2}} H^+ + HCO_3^- \tag{32}$$

$$HCO_3^- \xleftrightarrow{k_3, k_{-3}} H^+ + CO_3^{2-} \tag{33}$$

$$CO_2 + OH^- \xleftrightarrow{k_4, k_{-4}} HCO_3^- \tag{34}$$

$$HCO_3^- + OH^- \xleftrightarrow{k_5, k_{-5}} CO_3^{2-} + H_2O \tag{35}$$

where k_n and k_{-n} are rate constants of the forward and backward reactions for reaction n. K_n is the equilibrium constant of reaction n, $(K_n = k_n / k_{-n})$, which is given as a function of temperature according to the Van't Hoff equation

$$K_n = \exp\left(\frac{\Delta S_n}{R}\right) \exp\left(-\frac{\Delta H_n}{RT}\right) \tag{36}$$

with ΔS_n the change of entropy and ΔH_n the change of enthalpy of reaction n. The source term of each species due to these homogeneous reactions can then be calculated as

$$R_{\mathrm{B},j} = \varepsilon_{\mathrm{I}} \sum_n \nu_{j,n} \left(k_n \prod_{\nu_{j,n<0}} c_j - k_{-n} \prod_{\nu_{j,n>0}} c_j \right) \tag{37}$$

where ε_{I} is the volume fraction of the electrolyte, $\nu_{j,n}$ is the stoichiometric coefficient of species j for reaction n, and c_j is the dissolved species concentration.

2.5. Dissolved species transport

The molar flux of dissolved species (CO_2, H^+, OH^-, HCO_3^-, CO_3^{2-}) is calculated with the Nernst-Planck equation

$$\mathbf{N}_j = -D_j^{\mathrm{eff}} \nabla c_j - z_j F \frac{D_j^{\mathrm{eff}}}{RT} c_j \nabla \phi_{\mathrm{L}} \tag{38}$$

where D_j^{eff} is the effective diffusion coefficient in the ionomer of species j, z_j is the species charge and c_j is its concentration. The electroneutrality constraint is also applied to calculate the K^+ concentration in the electrolyte phase, which is accurate over lengths that exceed the double layer thickness of a few nanometers

$$c_{\mathrm{M}} + \sum_j z_j c_j = 0 \tag{39}$$

where c_{M} is the fixed charge concentration within the electrolyte phase. The diffusion coefficients of species in the electrolyte phase ($D_{j,\mathrm{M}}$) are calculated from Grew et al. [15,16]

$$D_{j,\mathrm{M}} = \epsilon_{\mathrm{w}}^q \frac{D_j}{x_{\mathrm{w}}(1+\psi_j)} \tag{40}$$

where ϵ_{w}^q is the water volume fraction in the membrane, q is the membrane tortuosity parameter, D_j is the diffusion coefficient of j in pure water, x_{w} is the mole fraction of water in the membrane, and ψ_j is the ratio of species/water to species/membrane interaction. ψ_j is approximated from kinetic theory by

$$\psi_j = \frac{1}{\lambda} \left(\frac{V_{\mathrm{M}}}{V_{\mathrm{w}}} \right)^{2/3} \left(\frac{M_{j,\mathrm{M}}^*}{M_{j,\mathrm{w}}^*} \right)^{1/2} \tag{41}$$

where λ is the membrane water content, defined as number of water molecules per charged group, V_{M} is the membrane molar volume, V_{w} the molar volume of water, and $M_{j,\mathrm{M}}^*$, $M_{j,\mathrm{w}}^*$ is the reduced molar mass calculated as

$$M_{j,h}^* = \left(\frac{1}{M_j} + \frac{1}{M_h} \right)^{-1} \quad h = \mathrm{M}, \mathrm{w} \tag{42}$$

where M_j is the molar mass of species j, M_{w} the molecular mass of water, and $M_{\mathrm{M}} = 1/\mathrm{IEC}$ the molecular mass of the membrane. The mole fraction of water in the membrane and the volume fraction of water are calculated as

$$x_{\mathrm{w}} = \frac{\lambda}{1+\lambda} \tag{43}$$

$$\epsilon_{\mathrm{w}} = \frac{\lambda V_{\mathrm{w}}}{V_{\mathrm{M}} + \lambda V_{\mathrm{w}}} \tag{44}$$

2.6. Gas transport

Gas transport in the CL and DM is modeled using the mixture-averaged model derived from the Stefan-Maxwell framework. The diffusive mass flux of gaseous species i is calculated with

$$\mathbf{j}_i = -\rho_{\mathrm{G}} D_i^{\mathrm{eff}} \nabla \omega_i - \rho_{\mathrm{G}} \omega_i D_i^{\mathrm{eff}} \frac{\nabla M_n}{M_n} \tag{45}$$

where ρ_{G} is the total gas density, D_i^{eff} is the effective diffusion coefficient, ω_i is the weight fraction of species i, and $M_n = \sum_i \left(\frac{\omega_i}{M_i} \right)^{-1}$ is the mixture average molecular weight. The diffusion coefficient of species i is calculated based on the contributions by the species-species diffusion coefficient (D_i^{SM}) and the Knudsen diffusion coefficient (D_i^{K})

$$D_i = \left(\frac{1}{D_i^{\mathrm{SM}}} + \frac{1}{D_i^{\mathrm{K}}} \right)^{-1} \tag{46}$$

where $D_i^{\mathrm{SM}} = \frac{1-\omega_i}{\sum_{n \neq i} \frac{y_n}{D_{i,n}}}$ and $D_i^{\mathrm{K}} = \frac{2 r_{\mathrm{pore,d}}}{3} \sqrt{\frac{8RT}{\pi M_i}}$.

Where y_n is the gas mole fraction, $D_{i,n}$ is the binary diffusion coefficient between species i and n, and $r_{\mathrm{pore,d}}$ is the average pore radius within domain d. The binary diffusion coefficient is determined as [17]

$$D_{i,n}\left[\mathrm{cm^2 s^{-1}}\right] = \frac{10^{-3} T[\mathrm{K}]^{1.75} \left(M_i\left[\mathrm{g\ mol^{-1}}\right]^{-1} + M_n\left[\mathrm{g\ mol^{-1}}\right]^{-1} \right)^{0.5}}{p_{\mathrm{G}}[\mathrm{atm}] \left(v_{\mathrm{P},i}^{0.33} + v_{\mathrm{P},n}^{0.33} \right)^2} \tag{47}$$

where p_{G} is the total gas pressure, and $v_{\mathrm{P},i}$ is the diffusion volume of species i.

2.7. Water transport

The model used to describe the water flux was derived from concentrated solution theory by Weber et al. for Nafion CEMs [18–20]. The molar water flux is given by

$$\mathbf{N}_{\mathrm{w}} = -\alpha_{\mathrm{w}}^{\mathrm{eff}} \nabla \mu_{\mathrm{w}} + \sum_j \xi_j \mathbf{N}_j \tag{48}$$

where $\alpha_{\mathrm{w}}^{\mathrm{eff}}$ is the effective water transport coefficient in the membrane, μ_{w} is the chemical potential of water in the membrane, and ξ_j is the electro-osmotic drag coefficient (EOC) for ion j. The chemical potential of water is given by

$$\mu_{\mathrm{w}} = RT \ln a_{\mathrm{w}} + V_{\mathrm{w}}(p_{\mathrm{M}} - p^{\mathrm{ref}}) \tag{49}$$

where a_{w} is the activity of water in the membrane, p_{M} is the liquid water pressure in the membrane, and p^{ref} is the reference pressure of 1 atm. To estimate the liquid water pressure, we assume the chemical potentials of the liquid and vapor sections equal, arriving at

$$p_{\mathrm{M}} = \begin{cases} \frac{\mu_{\mathrm{w}}}{V_{\mathrm{w}}} + p^{\mathrm{ref}}, & \text{if } \frac{\mu_{\mathrm{w}}}{V_{\mathrm{w}}} + p^{\mathrm{ref}} \geq 0 \\ 0, & \text{otherwise} \end{cases} \tag{50}$$

$$a_{\mathrm{w}} = \exp\left(\frac{\mu_{\mathrm{w}} - V_{\mathrm{w}}(p_{\mathrm{M}} - p^{\mathrm{ref}})}{RT} \right) \tag{51}$$

The fraction of pores that are liquid filled in equilibrium is calculated through [19]

$$S_{\mathrm{M}} = \frac{1}{2} \left[1 - \mathrm{erf}\left(\frac{\ln\left(\frac{-2\gamma \cos 90.02}{p_{\mathrm{M}}} \right) - \ln 1.25}{0.3\sqrt{2}} \right) \right] \tag{52}$$

where γ is the surface tension of water. The value of S_{M} determines the relative contributions of the liquid and vapor-equilibrated transport modes to the overall transport coefficient through

$$\alpha_{\mathrm{w}}^{\mathrm{eff}} = S_{\mathrm{M}} \alpha_{\mathrm{L}} + (1 - S_{\mathrm{M}}) \alpha_{\mathrm{V}} \tag{53}$$

where α_L is the liquid-equilibrated transport coefficient, and α_V is the vapor-equilibrated transport coefficient. The transport coefficients are defined as [19]

$$\alpha_V = \frac{c_w D_w}{RT(1-x_w)} \tag{54}$$

$$\alpha_L = \frac{k_M^{sat}}{\eta_w V_w^2}\left(\frac{\epsilon_w}{\epsilon_{w,max}}\right)^2 \tag{55}$$

where c_w is the water concentration in the membrane, D_w is the diffusion coefficient of vapor-equilibrated membrane, k_M^{sat} is the membrane saturated permeability, η_w is the dynamic viscosity of water. The concentration of water is calculated assuming free swelling with

$$c_w = \frac{\lambda}{V_w\lambda + V_M} \tag{56}$$

The water content in the membrane depends on whether the membrane is contacted with liquid water or vapor (Schröders paradox) and is calculated as

$$\lambda = \lambda_L S_M + \lambda_V(1-S_M) \tag{57}$$

where λ_V is the vapor equilibrated water content, and λ_L is the liquid equilibrated water content, which are provided in Table S1. Due to limited data availability for the EOC of specific ions, Weng et al. [3] used an average value and determined the overall EOC (ξ_A) as

$$\xi_A = \xi_L S_M + \xi_V(1-S_M) \tag{58}$$

Hence, the second term in Eq. (45) is replaced with

$$\sum_j \xi_j \mathbf{N}_j = -\xi_A \frac{\mathbf{i}_L}{F} \tag{59}$$

2.8. Heat transport

The heat transport equation is given as

$$\nabla.\left(-k_{T,d}^{eff}\nabla T\right) = Q_{CT} + Q_B + Q_{PT} + Q_J \tag{60}$$

where $k_{T,d}$ is the effective thermal conductivity of domain d, Q_{CT} is the volumetric heat source due to charge transfer reactions, Q_B is the heat source due to homogeneous reactions, Q_{PT} is the heat source due to phase transfer, and Q_J is the heat source due to ohmic heating.

The effective thermal conductivity in each domain is calculated by averaging the respective thermal conductivities of each phase. For the membrane

$$k_{T,M} = \epsilon_w k_{T,w} + (1-\epsilon_w)k_{M,dry} \tag{61}$$

where $k_{T,w}$ is the thermal conductivity of pure water, and $k_{M,dry}$ is the thermal conductivity of the dry membrane. For all other domains

$$k_T^{eff} = k_{T,S}^{bulk} + \varepsilon_G k_{T,G} + \varepsilon_L k_{T,w} + \varepsilon_I k_{T,M} \tag{62}$$

where $k_{T,S}^{bulk}$ is the dry bulk thermal conductivity of domain d, $k_{T,G}$ is the thermal conductivity of the humidified air.

Heating due to charge transfer reactions has two different contributions, one for irreversible heating and one for reversible heating.

$$Q_{CT,irr} = \sum_k i_{v,k}\eta_k \tag{63}$$

$$Q_{CT,rev} = \sum_k i_{v,k}\Pi_k \tag{64}$$

Here Π_k is the Peltier coefficient for reaction k. The Ohmic heating for the solid and liquid phases are given as

$$Q_{Ohmic,L} = \frac{\mathbf{i}_L^2}{\sigma_L^{eff}} \tag{65}$$

$$Q_{Ohmic,S} = \frac{\mathbf{i}_S^2}{\sigma_S^{eff}} \tag{66}$$

where the electrolyte effective conductivity (σ_L^{eff}) is calculated as

$$\sigma_L^{eff} = \frac{F^2}{RT}\sum_j z_j^2 c_j D_j^{eff} \tag{67}$$

Heat generation by the homogeneous reactions is expressed by

$$Q_{HR} = -\varepsilon_I \sum_n \Delta H_n \left(k_n \prod_{\nu_{n,j}<0} c_j^{-\nu_{n,j}} - k_{-n}\prod_{\nu_{n,j}>0} c_j^{\nu_{n,j}}\right) \tag{68}$$

where ΔH_n is the enthalpy change of reaction n. The heat source due to condensation/evaporation of water is

$$Q_{PT} = \Delta H_{w,vap}\, R_{w,PT} = \Delta H_{w,vap}\left(R_{w,G\to I} + R_{w,G\to L}\right) \tag{69}$$

where $R_{w,PT}$ is the phase transfer rates.

2.9. Phase transfer

The molar rate of phase transfer of CO_2 from the gas phase to the ionomer is calculated as

$$R_{PT,CO_2} = a_{v,COER}\, k_{MT,CO_2}\left(p_G\, y_{CO_2} H_{CO_2} - c_{CO_2}\right) \tag{70}$$

where k_{MT,CO_2} is the mass transfer coefficient and H_{CO_2} is Henry's constant for CO_2.

Phase transfer of water occurs between three different phases: the gas phase, the liquid phase, and the ionomer phase. For transfer from the gas phase to the ionomer

$$R_{w,G\to I} = a_v\, k_{MT,V}\left(\frac{RH}{100} - a_w\right) \tag{71}$$

where $k_{MT,V}$ is the water vapor mass transfer coefficient. Phase transfer of water from the liquid phase to the ionomer is calculated with

$$R_{w,L\to I} = a_v \frac{k_{MT,L}}{RT}(p_L - p_m) \tag{72}$$

where $k_{MT,L}$ is the liquid water mass transfer coefficient. Furthermore, water condensation and evaporation occur between the liquid and gas phases. The phase transfer of water from gas to liquid phase can occur in both the CL and the DM and is given by

$$R_{w,d,G\to L} = k'_{MT}(RH - 100\%)\left[H_0\left(\frac{p_L}{1[Pa]}\right)(S_d - S_{d,res}) + H_0(RH - 100\%)\right] \tag{73}$$

where k'_{MT} is an arbitrarily large mass transfer coefficient to ensure equilibrium between gas and liquid phases, H_0 is the Heaviside step function centered at zero, $S_{d,res}$ is the residual water saturation in domain d, which is the minimum water saturation taken from the capillary pressure-saturation curves. Eq. (73) ensures that as long as (1) the liquid pressure p_L is positive, (2) the liquid saturation S_d is larger than $S_{d,res}$, and (3) the relative humidity RH in the gas phase is less than 100%, water will evaporate. This process will continue until the relative humidity is 100%. The second term ensures that whenever the relative humidity exceeds 100%, condensation occurs. The gas phase mass balance involves the phase transfer of CO_2 and H_2O, and the production of H_2 and CO due to the charge transfer reactions

$$\Phi_G = -M_{CO_2} R_{PT,CO_2} - M_w \left(R_{w,m,G\to L} + R_{w,G\to I} \right) + \sum_{i\neq CO_2,H_2O} M_i R_{CT,i} \quad (74)$$

For the liquid phase, only the phase transfer of liquid water contributes the total volumetric mass source

$$\Phi_L = M_w \left(R_{w,d,G\to L} - R_{w,L\to I} \right) \quad (75)$$

2.10. Boundary conditions

The electrode potential ϕ_S is zero at the DM/CH boundary and set to the applied cell potential at the anode (varied from 2 V to 3.1 V). The dissolved species have a no-flux condition at the CL/DM boundary, while the anode boundary has a fixed concentration boundary determined by considering the Donnan potential defined as,

$$c_j^M = c_j^E \exp\left(-\frac{z_i F}{RT} \Delta\phi_D \right) \quad (76)$$

where c_j^M is the concentration of species j in the membrane, c_j^E is the concentration in the exchange solution, and $\Delta\phi_D = \phi_L^M - \phi_L^E$. $\Delta\phi_D$ is the Donnan potential, which is the electric potential difference at the interface between the membrane (ϕ_L^M) and the exchange solution (ϕ_L^E), caused by the fixed background charge of the AEM. The gas feed stream is 100% humidified CO_2. At the membrane/CL boundary, a no-flux condition is applied for the gaseous species. The gas pressure p_G is set to 1 atm in the gas channel (CH), and a no-flow boundary condition is set at the AEM/CL interface, assuming the gas phase does not penetrate the membrane. The porous DM will maintain a pressure imbalance between liquid and gaseous phases due to capillary forces. Once $p_L > p_G$ an outward flux at the DM/CH interface is assumed, with an arbitrarily large mass transfer coefficient to maintain pressure balance.

$$\mathbf{n}_w = \rho_w \mathbf{u} = 1\ \mathrm{kg\ m^{-2} s^{-1}} \left(\frac{p_L - p_G}{1[Pa]} \right) H_0 \left(\frac{p_L - p_G}{1[Pa]} \right) \quad (77)$$

For the water transport in the membrane, the chemical potential is set to zero at the anode, and a no-flux condition is applied at the CL/DM interface. The liquid pressure at the anode is assumed to be 1 atm.

Heat transfer at the anode and DM/CH boundary is modeled with a heat flux, where heat transfer coefficients were fitted with the results reported by Hurkmans et al. [21],

$$\mathbf{q} = h_T (T - T_{op}) \quad (78)$$

where T_{op} is the inlet temperature of the liquid anolyte and gas feed, i.e., 293.15 K.

3. Results and discussion

3.1. Ion distribution and ionic conduction

The ion distribution within the membrane and catalyst layer is evaluated in terms of the anionic fraction (Fig. 2a–c), defined as

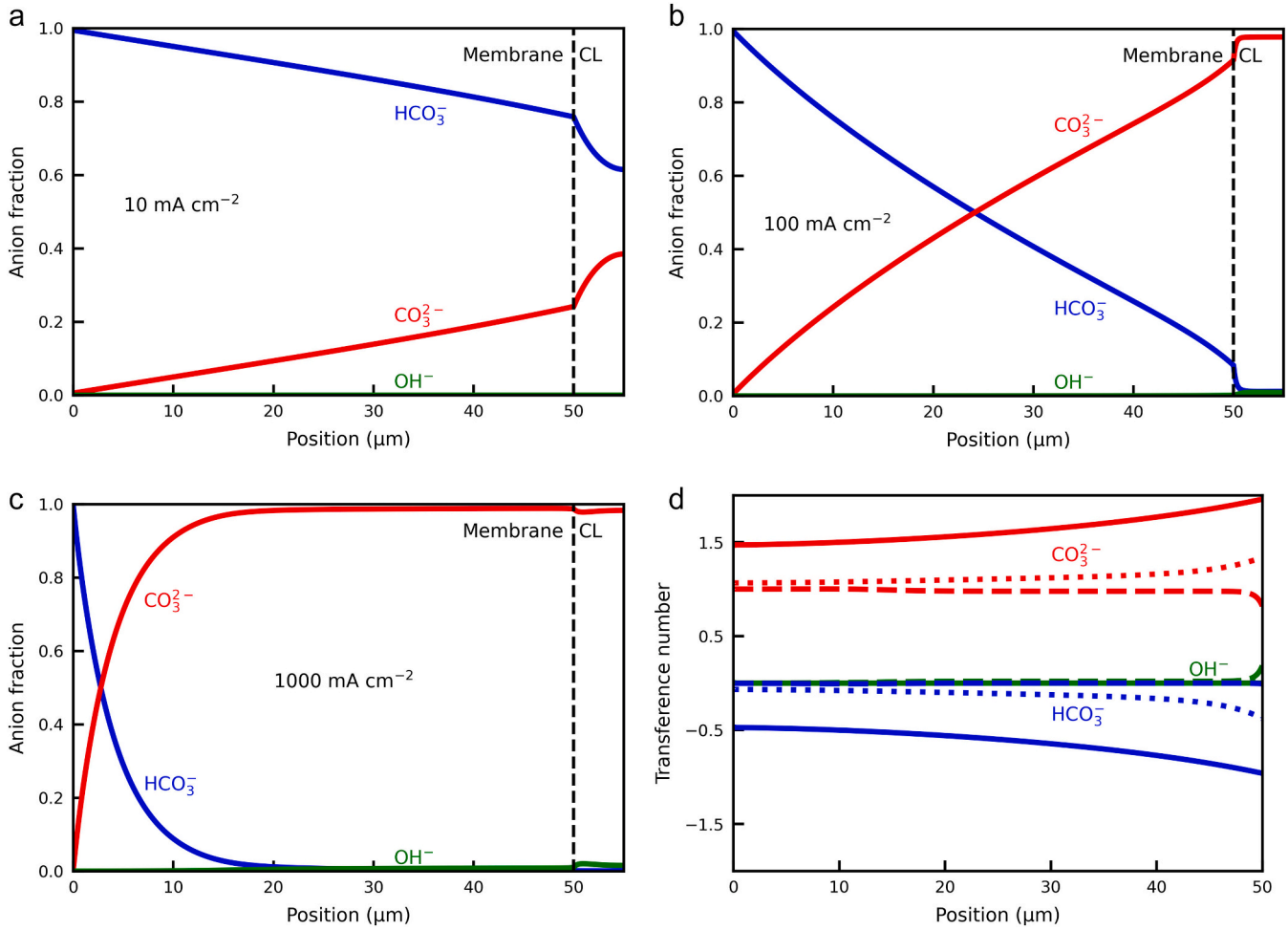

Fig. 2. The anion fractions in the membrane and CL as a function of position at current densities of (a) 10 mAcm^{-2} (b) 100 mAcm^{-2} and (c) 1000 mAcm^{-2}. The dashed line indicates the membrane/CL interface. (d) The transference numbers of the anions as function of position in the membrane at three different current densities (solid lines 10 mA cm^{-2}, dotted lines 100 mA cm^{-2} and dashed lines 1000 mA cm^{-2}).

$c_j/\left(c_{HCO_3^-}+c_{CO_3^{2-}}+c_{OH^-}\right)$. The corresponding concentration profiles of each ion are shown in Fig. S3. At low current densities, the membrane predominantly contains HCO_3^- (Fig. 2a), as bicarbonate is the main anionic species in the anolyte. As the current density increases, both the CO evolution reaction and hydrogen evolution reaction generate OH^-. This results in an increase in local pH within the catalyst layer and across the membrane (Fig. S3d). The homogeneous reactions (Eqs. (34) and (35)) convert dissolved CO_2 into HCO_3^- and subsequently into CO_3^{2-} in the presence of OH^-. Consequently, at a current density of 100 mA cm^{-2}, the membrane exhibits a gradient in composition: predominantly HCO_3^- near the anode side, and mostly CO_3^{2-} toward the cathode side (Fig. 2b). At a higher current density of 1000 mA cm^{-2}, the membrane contains almost entirely CO_3^{2-} (Fig. 2c), with a slight increase in OH^- fraction observed within the CL.

Fig. 2d shows the anion transference numbers in the membrane, defined as $(z_jFN_j)/i_L$, which represent the fraction of total ionic current carried by ionic species *j*. A positive transference number indicates that the ion contributes to charge transport in the direction of the electric current, whereas a negative value shows charge transport against the current. At a low current density of 10 mA cm^{-2}, the transference number for CO_3^{2-} ranges from 1.5 to 2, while that for HCO_3^- is between −0.5 and − 1. This indicates that HCO_3^- carries charge that counters the electric current, driven by its concentration gradient, which arises due to the conversion of HCO_3^- to CO_3^{2-}. The transference number of CO_3^{2-} exceeds unity to compensate for the transport of HCO_3^- against the current. As the current density increases, the transference number for CO_3^{2-} converges to approximately 1, while those for HCO_3^- and OH^- approach zero, consistent with their reduced presence as shown in the anion fraction profiles (Fig. 2c).

Notably, OH^- does not significantly contribute to ionic conduction in the membrane at any current density. Comparing this to the model developed by Lees et al. [9], a clear divergence is observed. Their model shows similar results at 10 mA cm^{-2}. However, at higher current densities, they predict a decrease in the CO_3^{2-} transference number from 2 to 0, while the OH^- transference reaches unity across the membrane at 1000 mA cm^{-2}, indicating OH^- as the dominant charge carrier. A key difference in their approach lies in the incorporation of a correction to CO_2 solubility in the ionomer to account for the salting-out effect. Additionally, their phase transfer coefficient for CO_2 from the gas phase to the ionomer (k_{MT,CO_2}) is two orders of magnitude lower than the value considered in this study. Both factors reduce the predicted CO_2 concentration within the ionomer and are further compared in the following paragraph.

The reduced CO_2 concentration in the CL ionomer limits the rate at which OH^- is consumed and CO_3^{2-} is generated via homogeneous reactions. As a result, the electrochemical generation of OH^- can exceed its consumption, leading to conversion of the membrane into an OH^- form. To investigate this effect, the CO_2 solubility correction applied by Lees et al. [9] was implemented, and the CO_2 gas-to-ionomer mass transfer coefficient was reduced to the value used in their study. These modifications led to similar CO_2 concentration profiles and ion transference behavior as observed by Lees et al. [9], as shown in Fig. S5. The CO_2 concentration profiles with the parameters used in this study (Table S1) are shown in Fig. S4. Experimental measurements of anode gas composition confirm that CO_3^{2-} is the dominant charge carrier in both Sustainion and PiperION membranes employed in exchange-MEA configurations for CO_2 reduction [22,23]. Hence, it is unclear if the CO_2 solubility correction is appropriate in this context. The values Lees et al. [9] used to estimate reduced CO_2 solubility are based on data from water/salt solutions, which may not accurately reflect the behavior of CO_2 in the ionomer phase [24], as the membrane used in their simulations (Sustainion) has been reported to have a CO_2 solubility approximately 20 times higher than that in water [25]. Additionally, the k_{MT,CO_2} applied by Lees et al. [9] is estimated based on experimental data for a 0.1 M KOH solution. Conversely, the model in this study does not account for the decrease in reactant CO_2 available for the CO_2R due to salt formation and the resulting CO_2 blockage. This needs further investigation since the GDE flooding initially caused by the salt formation dissolves $KHCO_3$ and allows CO_2 recovery at the CL [26]. Hence, a more relevant conclusion is CO_2 transport can be limited by salt precipitation or electrode flooding – leading to a transition to an OH^- form membrane. However, these effects are primarily driven by mass transport limitations rather than solubility constraints [26]. Knowing the ions profiles in the ionomer, in the next section we investigate water transport and different components of water flux in the ionomer.

3.2. Dominant water transport mechanisms

At lower current densities (10–100 mA cm^{-2}) the water flux through the membrane is negative, meaning net water is transported from the cathode to the anode. As the current density increases, the water flux becomes positive and continues to rise with increasing current density (Fig. 3a). Note that the sharp variation in water flux near the CL is caused by homogeneous reactions, in which water is either consumed or generated.

The water flux components driven by the chemical potential gradient and electro-osmotic drag act in opposite directions (Fig. 3b). As the current density increases, the electro-osmotic flux also increases. To sustain the water flux required by the CL, a negative chemical potential gradient is established across the membrane. For a liquid-equilibrated membrane, this results in a reduction of liquid pressure in both the membrane and the CL, which in turn lowers the capillary pressure in the CL and decreases the liquid saturation of the pores (Fig. S6a and b). Similar results were shown by Weng et al. [3] for the liquid pressure gradient and water saturation in the CL.

The water flux through the membrane can be normalized by the water consumption required by the electrochemical reactions. This normalized water flux, denoted by $\beta = N_w/(i_L/F)$, is commonly used in fuel cell studies to assess the impact of water transport on performance [14,27]. In hydroxide exchange membrane fuel cells (HEMFCs), a β value of 0.5 in the membrane indicates that just enough water is supplied to sustain the electrochemical reaction [14]. Previous work that applied this concept to evaluate water transport in an exchange-MEA used for CO_2RR suggested that a negative β value indicates water is primarily sourced from the humidified CO_2 stream, whereas a positive β suggests that the water reactant is supplied by the anolyte [9]. We calculated β values for different current densities (shown in Fig. S7). At current densities below 100 mA cm^{-2}, β is negative; it becomes positive at higher current densities. According to the relatively small magnitude of β, the water supply remains insufficient to fully sustain the COER; however, below we explain that β may not be a suitable parameter to assess the water transport in CO_2 electrolyzers.

A comprehensive water balance across the entire domain is presented in Fig. 4a, comparing the water flux at the anode boundary (x = 0 μm) with the flux at the DM/CH boundary (x = 380 μm). The water flux is defined as positive when directed from the anode toward the cathode channel. At low current densities, the water flux at the anode boundary is outward, exiting the cell. At a current density of around 130 mA cm^{-2}, the flux becomes inward, increasing further with rising current density. At the DM/CH boundary, the water flux remains outward at all current densities. The difference between these two fluxes represents the net water flux consumed within the cell. An outward water flux at the DM/CH suggests that the humidified CO_2 stream is not the water source for the electrochemical reactions. However, at low current densities, the water is neither supplied from the anode. Surprisingly, the net water consumption is negative at low current densities, indicating that water is produced within the cell.

To further analyze this behavior, the net water consumption is normalized by the stoichiometric water requirement of the electrochemical reactions, resulting in the relative water consumption shown in Fig. 4b. At current densities below 130 mA cm^{-2}, water is produced in

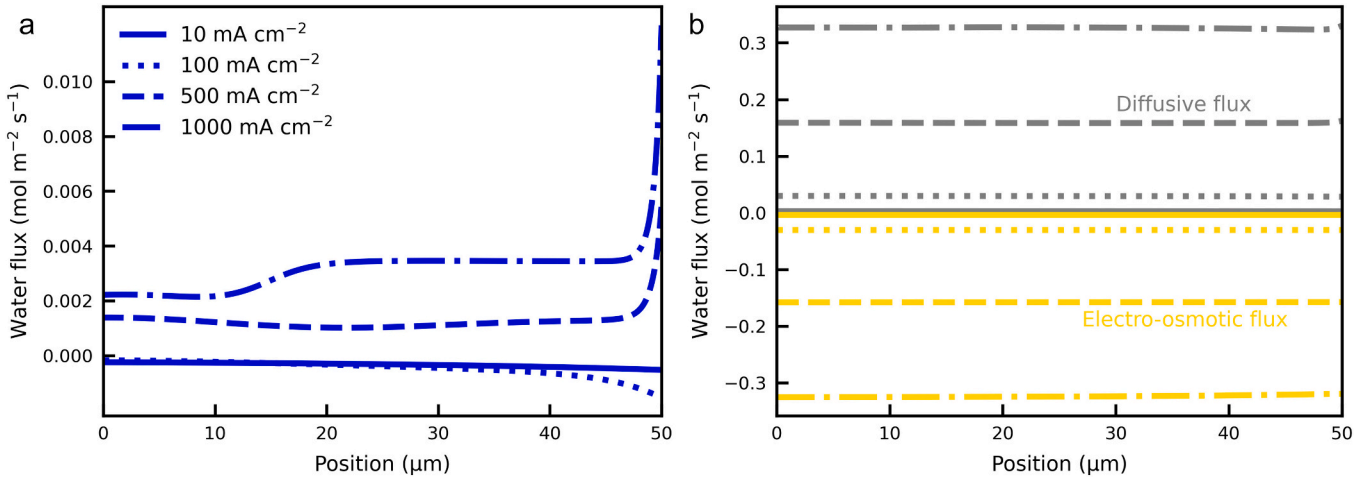

Fig. 3. (a) The total water flux throughout the membrane for different current densities. (b) The diffusive chemical potential driven water flux (grey) and the electro-osmotic water flux (yellow) at different current densities: solid lines 10 mAcm^{-2}, dotted lines 100 mAcm^{-2}, dashed lines 500 mAcm^{-2}, and dash-dotted lines 1000 mAcm^{-2}.

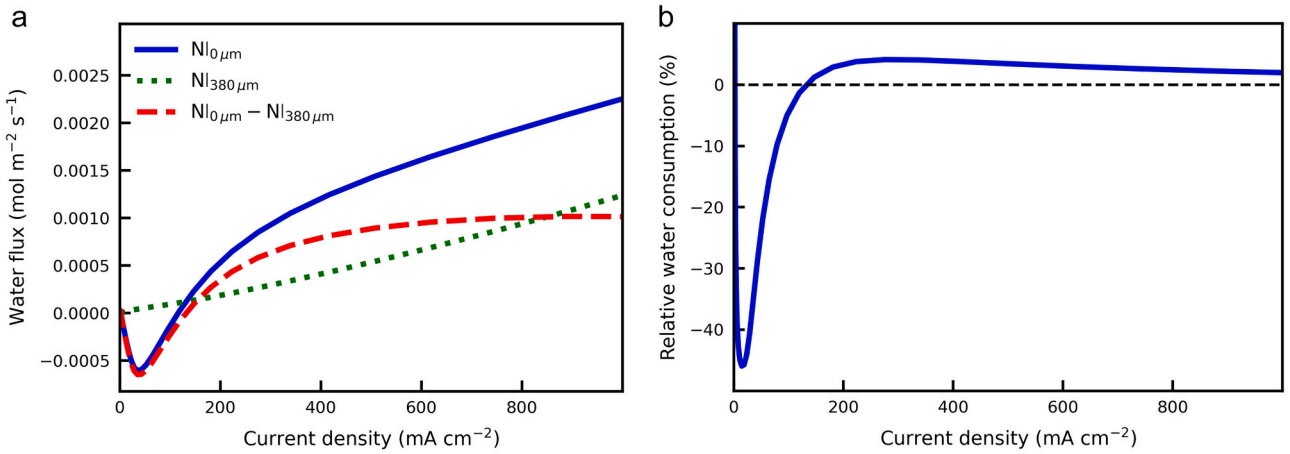

Fig. 4. (a) Water balance on the entire domain, by comparing the flux at the anode/membrane boundary, DM/CH boundary and the net consumption of water. (b) Relative water consumption, i.e., net water consumption flux normalized by the stoichiometric amount required by the electrochemical reactions.

excess – up to 46% more than the stoichiometric demand. A balance point is reached at 130 mA cm^{-2}. At higher current densities, the relative water consumption remains below 5% of the stoichiometric requirement and gradually decreases as the current density increases.

These figures highlight the importance of homogeneous reactions in the overall water balance, as these are the only mechanisms capable of reducing net water consumption through water production. At low current densities ($i < 130$ mA cm^{-2}), there is a large flux of HCO_3^- toward the cathode. The homogeneous reaction producing CO_3^{2-} (Eq. (35)) dominates due to its higher rate constant compared to the reaction that forms HCO_3^- (Eq. (34)). The overall net reduction reaction is then the sum of the COER and the CO_3^{2-}-producing buffer reaction

$$CO_2 + 2HCO_3^- + 2e^- \rightarrow 2CO_3^{2-} + CO + H_2O \quad (79)$$

This results in a net production of water, as shown in Fig. 4b. At higher current densities, HCO_3^- is depleted, first in the CL, and subsequently in the membrane (see Fig. S3b). This depletion limits the rate of the CO_3^{2-}-producing reaction, causing it to approach the rate of the HCO_3^- producing buffer reaction. The overall net reaction then becomes

$$2CO_2 + 2e^- \rightarrow CO_3^{2-} + CO \quad (80)$$

In this case, no net water is produced or consumed. Deviation from a perfectly balanced system is expected, as the buffer reactions are not at equilibrium. The sensitivity analysis shows that the $CO_2 + OH^- \rightleftharpoons HCO_3^-$ reaction is the dominant kinetic pathway controlling the buffer reactions water source. Thus, the water balance is highly sensitive to the value of k_4 (Fig. S9). This reaction directly controls the local OH^- concentration. The heat and mass transfer parameters do not affect the transition point, and they only impact the water flux and once the net reaction follows Eq. (80), the water balance may change based on the transfer coefficients.

At current densities above 130 mA cm^{-2}, the water flux entering the membrane increases with current density, whereas the flux required to sustain electrochemical consumption plateaus (Fig. 4a). This increasing flux is due to the rise in temperature of the CL (Fig. S8), which elevates the vapor pressure of the liquid water present and thereby increases the mole fraction of H_2O in the gas phase. As a result, the diffusive flux of H_2O toward the gas channel exceeds the convective flux toward the CL, leading to a net water transport out of the cell.

The relative humidity at the DM/CH boundary decreases due to the rise in temperature and the constant mole fraction of water, while it remains at 100% in the CL due to equilibration with the liquid water present. This indicates that at higher current densities, the temperature gradient, and not the electrochemical consumption of water, dominates the water flux across the cell. This was confirmed by running the model in isothermal mode, where the total water flux through the membrane matches the net water consumption or production.

Table 1
Water transport parameters assumed in continuum models.

α_L [mol^2/(J·cm·s)]	α_v [mol^2/(J·cm·s)]	Ref.	Notes
6.3×10^{-7}	6.3×10^{-9}	[3,21]	293 K
2×10^{-9}	2×10^{-9}	[9]	Sustainion, 50 °C
3×10^{-9}	3.4×10^{-10}	[14]	293 K

The removal of water by the CO_2 gas stream, contrary to the intended use of supplying water through humidification of the CO_2 gas, has also been reported experimentally [28–30]. The flattened net water flux profile indicates that the use of a humidified CO_2 feed may not be necessary at high current densities when a liquid anolyte is used, as suggested by Lees et al. [9]. They observed the opposite trend at intermediate current densities (the range where CO_3^{2-} was reported as the main charge carrier, i.e., 200 mA cm^{-2}), where H_2O vapor diffused into the CL. This is due to a lower Faradaic efficiency for CO in their model and a lower water transport coefficient in the membrane.

Our findings highlight the importance of coupling between heat transfer and water transport at high current densities, which has also been found to be significant in PEMFC [31]. The magnitude of this effect is sensitive to the boundary conditions for both heat and mass fractions at the DM/CH interface. Hurkmans et al. [21] included a 2D gas channel in their model and showed that exchange MEAs can experience up to a 10 K temperature increase along the flow direction. Therefore, the heat flux boundary condition used here is a conservative estimate. The effect is significant because water vapor pressure increases exponentially with temperature, amplifying the water mole fraction gradient and potentially enhancing the outward water flux. This flux can saturate the channel and elevate the H_2O mass fraction at the boundary. A 2D model is required to investigate this effect along the flow channel more accurately, as it depends strongly on the feed gas flow rate.

Our analysis helps clarify the discussion presented by Garg et al. [8] regarding the increasing water flux into the cathode with increasing current density, as experimentally reported by Reyes et al. [29].

Our results also show that in models where homogeneous water production contributes significantly, using the water balance coefficient β seems not to be suitable. However, for designs with a lower CO_2 solubility that limits homogeneous reaction rates, β might remain a valid metric [9]. In the next two sections we will investigate the effects of the membrane properties on the water balance and the mechanisms governing water transport.

3.3. Influence of membrane transport properties

Next, we investigate the influence of water transport parameters in the membrane to evaluate their effects on water balance and membrane hydration. The values of the water transport coefficients reported in modeling literature vary by orders of magnitude (see Table 1). On the other hand, the water diffusivity as a function of water content and temperature has been experimentally investigated for various AEMs, including Tokuyama A201 [32,33], HMT-PBMI [34], Fumapem FAA3 [34,35], and Piperion [35]. However, interpreting such measurements is challenging due to variations in experimental conditions and the presence of multiple transport mechanisms within the membrane. In particular, the decoupling of internal and external transport resistances is often neglected, which can be significant, especially for membranes exposed to vapor-phase conditions [22]. Table 2 shows experimentally measured water diffusivities in membranes, where the vapor-equilibrated water transport coefficient is calculated using Eq. (54).

To explore the range of water transport coefficients reported in the literature, we vary the effective transport coefficient from its original α value to 0.01α. The higher end of this range aligns with values used by Weng et al. [3] and Hurkmans et al. [21] (first row in Table 1), whereas the lower end, used in the modeling study by Gerhardt et al. [14] (last row in Table 1), is approximately two orders of magnitude smaller and better reflects experimentally measured values (Table 2).

Simultaneously, we perform a parametric study on the influence of the effective electro-osmotic coefficient by increasing ξ by a factor of 4. This adjustment aligns with recent measurements of ion transport numbers in AEMs by Petrovick et al. [36]. Since the membrane contains predominantly CO_3^{2-}, a higher electro-osmotic drag is expected, as CO_3^{2-} has a reported transport number of $\xi_{CO_3^{2-}} = 20$. In Fig. 5, (α, ξ) represents the hydrated case, i.e., a membrane with a low water transport resistance and a small electro-osmotic drag coefficient. The dehydrated case $(0.01\alpha, 4\xi)$ represents a membrane with a low water transport coefficient and high EOD. These two cases represent the two limits of operation (low versus high water transport resistance) and are hereafter referred to as the hydrated case and the dehydrated case, respectively.

The average water content in the membrane decreases with increasing current density. However, as shown in Fig. 5a the *extent* of membrane dehydration varies significantly between the cases. The hydrated case (α, ξ) shows full membrane hydration, even at high current densities. Increasing the electro-osmotic drag coefficient leads to partial membrane dehydration at high current densities. Significant dehydration occurs for the dehydrated case $(0.01\alpha, 4\xi)$ with lower water transport coefficient and higher EOD $(0.01\alpha, 4\xi)$.

Our results qualitatively agree with neutron imaging experiments by Dische et al. [30], who observed that membrane and cathode GDE dehydration increases with current density up to approximately 200 mA cm^{-2}, with drier conditions in the cathode GDE. The maximum current density achieved at 3.1 V decreases with increasing membrane dehydration, from 1400 mA cm^{-2} for the hydrated case to 900 mA cm^{-2} for the dehydrated case. This is due to the lower ionic conductivity in the dehydrated membrane, which increases the ohmic resistance.

On the anode side, the water content remains constant at its liquid-equilibrated value of $\lambda = 17$, and only decreases slightly in the hydrated case. In contrast, the dehydrated case exhibits a liquid-

Table 2
Water transport parameters measured experimentally for specific membranes.

D [m^2/s]	Membrane	Ref.	Method	T [°C]	α_v [mol^2/(J·cm·s)]
6×10^{-10}	Tokuyama A201	[32]	PFG-NMR	30	5.22×10^{-10}
3×10^{-10}	Tokuyama A201	[33]	LVP	30	2.61×10^{-10}
4.9×10^{-10}	HMT-PMBI	[34]	LVP	70	4.35×10^{-10}
2×10^{-10}	Fumapem FAA3	[34]	LVP	70	1.74×10^{-10}
5.2×10^{-10}	Fumapem FAA3	[35]	LVP	30	4.52×10^{-10}
2.4×10^{-10}	Piperion	[35]	LVP	30	2.10×10^{-10}

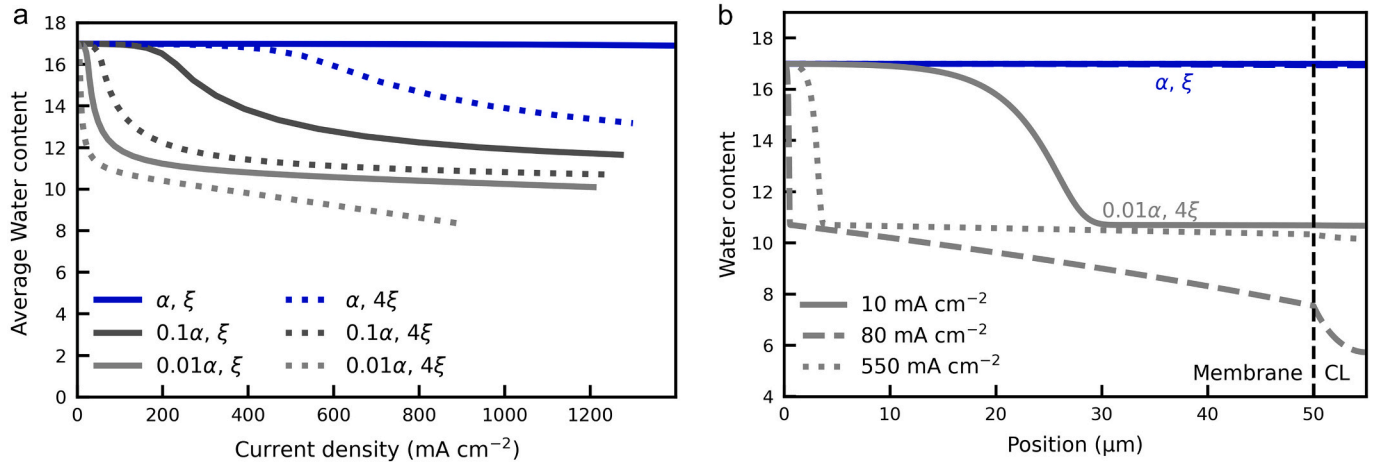

Fig. 5. (a) Average water content in the membrane as a function of current density for α to 0.01α, and ξ to 4ξ. (b) The water content profile throughout the membrane and CL for the hydrated case (α, ξ) and dehydrated case $(0.01\alpha, 4\xi)$.

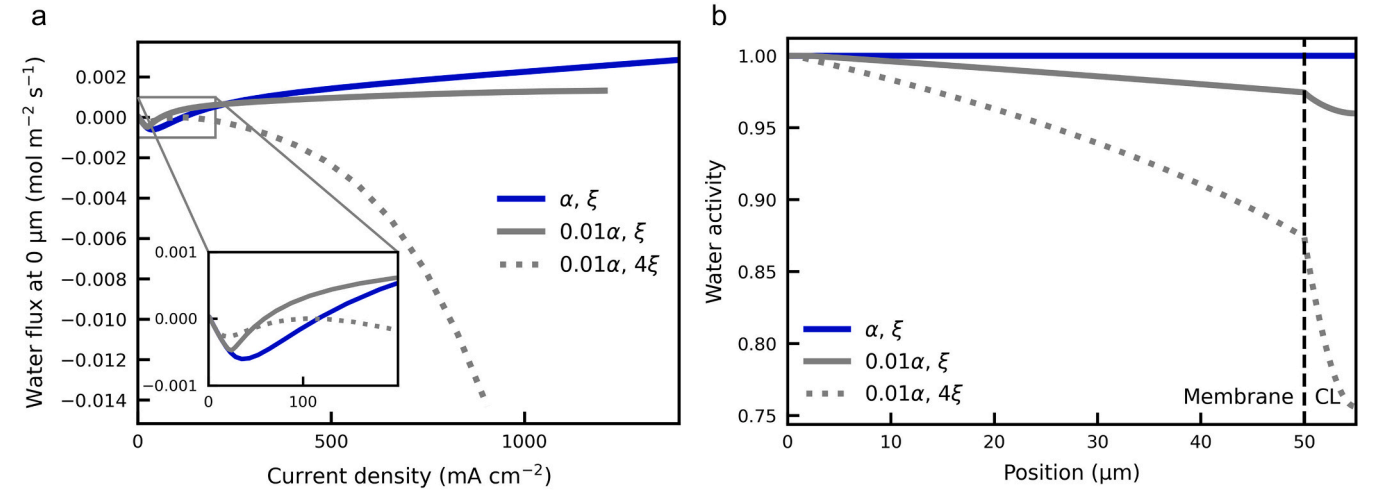

Fig. 6. (a) The water flux at the anode/membrane interface as a function of current density for the hydrated (magenta solid line), dehydrated (dotted line), and a case in between (grey solid line). The inset shows negative water fluxes at lower current densities. (b) The water activity in the membrane and CL at 600 mAcm^{-2} for same cases as in (a).

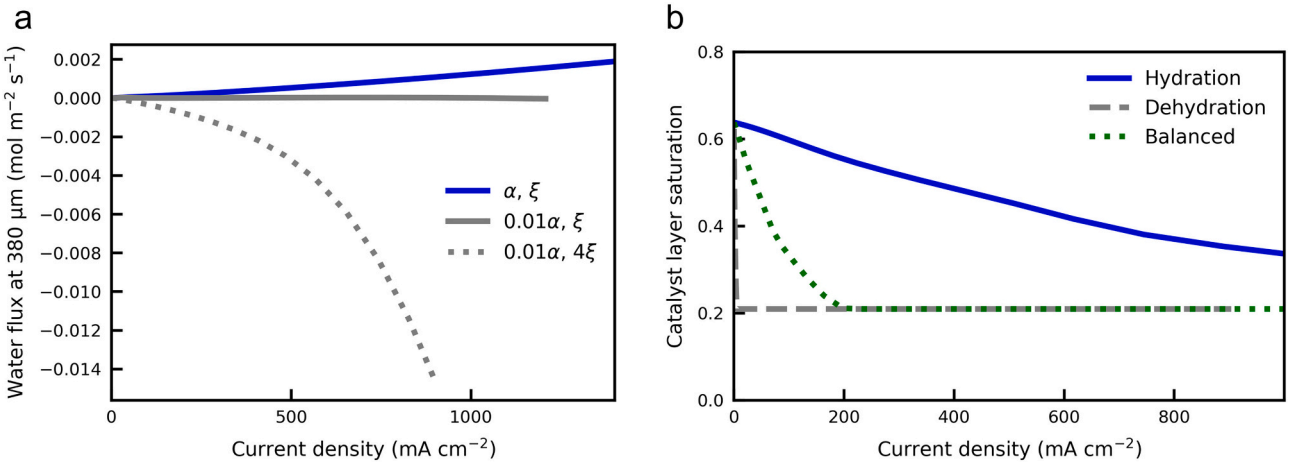

Fig. 7. (a) Excess water supplied to the cathode for the hydrated, dehydrated and balanced cases. (b) The CL saturation for the three cases as a function of current density.

equilibrated boundary layer near the anode, the thickness of which decreases with increasing current density (Fig. 5b). A sharp decrease in water content is observed at the transition from the liquid- to vapor-equilibrated state. This transition has a distinct shape, governed by the membrane's liquid equilibration curve, which accounts for Schröder's paradox. Once the membrane is fully vapor-equilibrated, the water content is determined by an activity-dependent sorption isotherm. Water content profiles for Nafion membranes have been experimentally investigated. While no abrupt drop in λ was reported, the presence of a liquid-equilibrated boundary layer was observed [37].

The transport parameters have a significant impact on the water balance, as evidenced by the contrasting trends in water flux at the anode/membrane boundary for the different cases (Fig. 6a). In the hydrated case, water flows into the membrane from the anode, while in the dehydrated case, the water flux is negative, indicating flow from the membrane into the anode. Notably, all cases exhibit an initial negative water flux at current densities below 100 mA cm^{-2} due to net water production, as discussed earlier. As the current density increases and the overall reaction stoichiometry shifts toward net water consumption, the direction of water flux reverses, and water flows into the membrane from the anode. However, in the dehydrated case, the CL dries out due to the lower water transport coefficient. The water activity in the CL ionomer decreases rapidly (Fig. 6b), driven by the combination of the low water transport coefficient and a high electro-osmotic drag coefficient, which pulls water from the gas phase into the membrane. This reduces the relative humidity in the CL. The combined effect outweighs the opposing water flux driven by the temperature gradient. This behavior is consistent with the results reported by Lees et al. [9], who reported similar drying effects in the CL for the gaseous H_2O transport under comparable transport parameter magnitudes. However, due to the reduced CO_2 concentration and higher Faradaic efficiency for H_2, their model exhibits a higher net water consumption. The additional water required is drawn from the membrane. In contrast, in the present model, water is produced and subsequently transported from the membrane to the anode. For the intermediate case between the hydrated and dehydrated cases $(0.01\alpha, \xi)$, the reduced water activity almost exactly counters the temperature gradient, resulting in no net water exchange between the gas phase and the ionomer (Fig. 7a). The water flux into the membrane from the anode matches the amount required by the electrochemical reaction at all current densities, highlighting a potential opportunity for balanced water management. Additionally, the saturation of the CL pores is strongly influenced by the transport parameters, as shown in Fig. 7b.

Our analysis reveals two distinct regimes based on membrane hydration (Figs. 6a and 7a). In the well-hydrated case, the water flux is driven by the temperature gradient across the catalyst layer and diffusion medium, resulting in water being pulled through the membrane, as discussed in the previous section. In contrast, in the dehydrated membrane the direction of the water flux is reversed. Water vapor is adsorbed into the membrane driven by a combination of higher electro-osmotic drag (EOD) and a lower water transport coefficient.

Hence for the dehydrated case, at low current densities net water consumption governs the water flux, the same as for the hydrated case. However, at higher current densities, the water flux is dominated by evaporation or adsorption into the membrane due to electro-osmotic drag.

3.4. Influence of membrane thickness

The membrane thickness has been reported to significantly influence cell performance, water balance, and cation accumulation at the cathode [29,38]. Here we investigate membrane thicknesses ranging from 20 to 80 μm. As expected, the average membrane water content increases with decreasing membrane thickness for both the hydrated and dehydrated cases (Fig. 8a). Additionally, the water saturation of the CL increases for thinner membranes, due to the higher water pressure in the CL, although experimental studies have attributed the improved performance in thin membranes to reduced flooding, based on measurements of H_2O flux into the gas channel [29].

The water balance analysis (Fig. 9a) shows that using a 80 μm thick membrane increases the water flux from the anode into the membrane compared to a 50 μm membrane (Fig. 6a). This flux rises with current density, due to the increased water evaporation. A thicker membrane results in a larger temperature increase in the catalyst layer, due to its larger heat transfer resistance (Fig. S8).

In contrast, the 20 μm thick membrane exhibits a water flux at the anode directed toward the anolyte compartment. The flux into the gas channel is lower than for the thicker membrane, due to faster heat dissipation through the thinner membrane. The convective and diffusive fluxes of water vapor balance out. The finding that thinner membranes reduce the observed water flux at the cathode gas channel aligns well with experimental results reported by Reyes et al. [29]. As shown in Fig. 9a, there is net water production in the cell at all current densities. Initially, net water production occurs due to the high concentration of HCO_3^- in the CL, which reacts with OH^- generated by electrochemical reactions (following Eq. (35)). As the HCO_3^- in the CL becomes depleted, the water production decreases, as the overall reaction stoichiometry shifts to Eq. (80). When the OH^- concentration continues to rise in the CL, it diffuses further into the membrane, where it reacts with HCO_3^- present on the anode side. This explains why thinner membranes exhibit changes in the net water consumption flux in Fig. 9a, whereas thicker membranes display a plateau. In thinner membranes, OH^- and HCO_3^-

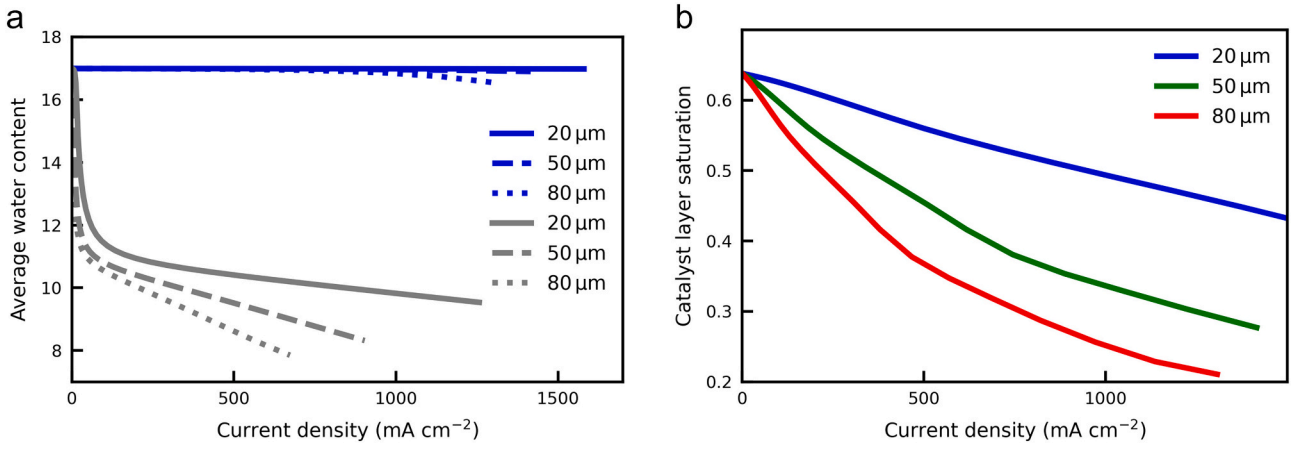

Fig. 8. (a) Average water content in the membrane for the hydrated (blue lines) and dehydrated (grey lines) cases as a function of current density for different membrane thicknesses. (b) Average water saturation in the catalyst layer as a function of current density for different membrane thickness (only for hydrated case).

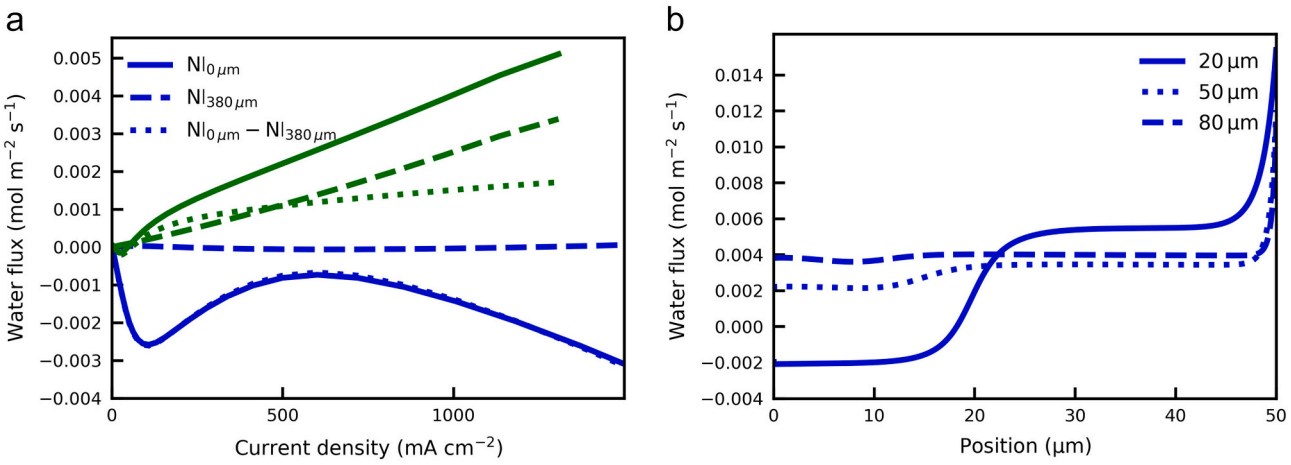

Fig. 9. (a) Water fluxes for membrane thicknesses of 80 µm and 20 µm. (b) Water flux profile throughout the membrane for different thicknesses at 3.05 V.

are in closer proximity, allowing them to react more readily within the membrane and produce water. As a result, the water balance in thinner membranes is governed by homogeneous reactions. In contrast, in thicker membranes, heat transport becomes the dominant factor influencing water flux.

In thin membranes, the water source term from homogeneous reactions contributes significantly, shifting the flux from negative at the anode side to positive at the cathode side (Fig. 9b). The results of catalyst layer saturation in Fig. 8b and water flux across the cell in Fig. 9a indicate that a lower water flux to the cathode gas channel (comparing fluxes at 380 µm) can coexist with higher CL saturation. This suggests that flooding observed in thicker membranes is more likely caused by salt formation, as proposed by Biemolt et al. [38]. However, definitive conclusions are limited by several uncertainties, including the potential role of electro-wetting effects in the CL and DM at higher cell potentials [13]. As such, no solid conclusions can be drawn regarding the direct influence of membrane thickness on flooding behavior.

3.5. A case with limited CO_2 in the cathode

Finding the prominent role of hydroxide ion in water balance, we examined whether deviations from a predominantly carbonate charge carrier in the membrane, arising from increased hydroxide concentrations under CO_2-limited cathode conditions affect the overall water balance. We simulated a CO_2-limited condition. While such conditions may vary between cells and depend on local concentrations and operating current, our objective is to illustrate how an increased hydroxide fraction in the membrane influences the water balance. As shown in Fig. S10, the membrane water flux changes significantly with increasing hydroxide fraction. Consequently, net water production is observed at high current densities, analogous to the low-current regime, following Eq. (79). Disch et al. [30] reported a decrease in normalized transmitted neutron intensity, defined as the relative change in neutron transmission with respect to the zero-current condition, which they attributed to salt formation based on the assumption of substantial water consumption at current densities between 200 and 300 mA cm^{-2}. In contrast, our results indicate that water can be produced within the cell via homogeneous reactions, particularly when hydroxide ions become more prevalent in the membrane.

4. Conclusion

The mechanisms governing water transport and balances in MEAs for CO_2RR are still not well understood. In this study, we developed a stationary one-dimensional, non-isothermal multiphysics model of a $KHCO_3$-exchange MEA CO_2 electrolyzer with a Tokuyama A201 anion exchange membrane to investigate the ion distribution and water transport under industrially relevant current densities. The model performance was validated with experimental data and reproduces cell performance up to 600 mA cm^{-2}.

The simulations highlight the important role of homogeneous reactions for the water balance in a MEA cell. For low current densities, homogeneous reactions produce more water than is consumed by the electrochemical reactions near the CL domain. In this regime, the reaction $HCO_3^- + OH^- \rightleftharpoons CO_3^{2-} + H_2O$ prevails due to the high fraction of bicarbonate present in the ionomer. For higher current densities, water production depends on the ionic composition of the membrane. If carbonate is the dominant charge carrier, the net consumption is less than 5% of the stoichiometric amount required. If the hydroxide ion increases in the membrane, for example under CO_2-limited cathode conditions, net water consumption in the cell decreases.

For a hydrated 50 µm AEM (α, ξ), at low current densities ($i < 130$ mA cm^{-2}), homogeneous buffer reactions dominate the water balance within the cell, resulting in net water production near the catalyst layer. At higher current densities ($i > 130$ mA cm^{-2}), the flux is governed by the temperature gradient over the cathode GDE. However, this changes for a dehydrated membrane with lower transport parameters and high EOD $(0.01\alpha, 4\,\xi)$, for which at high current densities the water flux is dominated by evaporation or adsorption into the membrane at CL. The water vapor diffuses from the channel to the catalyst layer, is subsequently absorbed into the membrane, and is transported to the anolyte by electro-osmosis. However, at higher current densities, if the hydroxide fraction in the membrane increases, hydroxide ions transport through the membrane and react with depleted bicarbonate near the anode, causing homogeneous reactions to govern the water balance over nearly the entire current density range.

Thin well-hydrated membranes (20 µm) were found to have a net production of water at all current densities within the membrane and ionomer domains, due to the shorter diffusion paths of HCO_3^- and OH^-. Water is transported from the membrane to the anode, and the flux increases with current density. Faster heat transport reduces the temperature in the CL, and no significant flux of water or water vapor is seen in the DM. Similar to the 50 µm membrane, for thick (80 µm) well-hydrated membranes, the temperature gradient dominates the water balance. However, the flux increases compared to the 50 µm membrane as thicker membranes result in larger temperature increases in the CL due to the larger heat transfer resistance.

In summary, our modeling work demonstrated homogeneous reactions govern the net reaction stoichiometry in the cell and are therefore necessary to consider for the water balance. For a membrane with carbonate as the dominant charge carrier the role of membrane transport parameters in determining MEA performance and water balance is

critical. The relative contribution of different mechanisms was shown to be dependent on membrane properties including transport parameters, electro-osmotic drag coefficients, and thickness. At current densities >130 mA cm^{-2}, the mechanism dominating the water flux changes from heat transfer in a well-hydrated membrane to electro-osmotic transport in a dehydrated membrane or to the homogeneous reactions in thin membranes. For lower current densities <130 mA cm^{-2}, the water production through the homogeneous reaction dominates the water flux. This work provides guidelines for water management in CO_2 electrolyzers by offering insight into the dominant physical processes governing water transport, with a focus on AEMs.

A two-dimensional model would provide a more accurate description of coupled thermal and mass transport effects, as the conservative heat flux boundary condition used here does not capture temperature variations along the flow channel that can significantly amplify vapor-driven water fluxes. Additionally, the contribution of homogeneous reactions, particularly those involving OH^- ions, is expected to become more significant at higher electrolyte concentrations due to increased water production, warranting further dedicated investigation.

CRediT authorship contribution statement

Nasim Heydari: Writing – review & editing, Writing – original draft, Visualization, Validation, Software, Methodology, Investigation, Formal analysis, Conceptualization. **Niels J. Böcker:** Writing – original draft, Software, Methodology, Investigation, Formal analysis. **David A. Vermaas:** Writing – review & editing, Software, Methodology. **Johan T. Padding:** Writing – review & editing, Validation, Supervision, Software, Methodology, Formal analysis. **J. Ruud van Ommen:** Writing – review & editing, Supervision, Project administration, Investigation, Funding acquisition.

Declaration of competing interest

The authors declare that they have no known competing financial interests or personal relationships that could have appeared to influence the work reported in this paper.

Acknowledgments

The authors would like to acknowledge the NWO for providing the FlexEChem Grant (NWA.1237.18.002) via the NWA-themed call “Opslag en conversie”. The authors acknowledge Akshaykumar Narsinhbhai Desai for insightful discussions on water management modeling.

Appendix A. Supplementary data

Supplementary data to this article can be found online at https://doi.org/10.1016/j.cej.2026.174240.

Data availability

Data will be made available on request.

References

[1] P. De Luna, C. Hahn, D. Higgins, S.A. Jaffer, T.F. Jaramillo, E.H. Sargent, What would it take for renewably powered electrosynthesis to displace petrochemical processes? Science 364 (6438) (2019) eaav3506, https://doi.org/10.1126/science.aav3506.

[2] A. Somoza-Tornos, O.J. Guerra, A.M. Crow, W.A. Smith, B.-M. Hodge, Process modeling, techno-economic assessment, and life cycle assessment of the electrochemical reduction of CO_2: a review, Iscience 24 (7) (2021) 102813, https://doi.org/10.1016/j.isci.2021.102813.

[3] L.C. Weng, A.T. Bell, A.Z. Weber, A systematic analysis of Cu-based membrane-electrode assemblies for CO_2 reduction through multiphysics simulation, Energ. Environ. Sci. 13 (10) (2020) 3592–3606, https://doi.org/10.1039/D0EE01604G.

[4] Carbon Dioxide | Vital Signs– Climate Change: Vital Signs of the Planet. https://climate.nasa.gov/vital-signs/carbon-dioxide/?intent=121 (accessed December 2025).

[5] C.P. O'Brien, R.K. Miao, A. Shayesteh Zeraati, G. Lee, E.H. Sargent, D. Sinton, CO_2 electrolyzers, Chem. Rev. 124 (7) (2024) 3648–3693, https://doi.org/10.1021/acs.chemrev.3c00206.

[6] M. Jouny, W. Luc, F. Jiao, General techno-economic analysis of CO_2 electrolysis systems, Ind. Eng. Chem. Res. 57 (6) (2018) 2165–2177, https://doi.org/10.1021/acs.iecr.7b03514.

[7] E.W. Lees, B.A. Mowbray, F.G. Parlane, C.P. Berlinguette, Gas diffusion electrodes and membranes for CO_2 reduction electrolysers, Nat. Rev. Mater. 7 (1) (2022) 55–64, https://doi.org/10.1038/s41578-021-00356-2.

[8] S. Garg, C.A.G. Rodriguez, T.E. Rufford, J.R. Varcoe, B. Seger, How membrane characteristics influence the performance of CO_2 and CO electrolysis, Energ. Environ. Sci. 15 (11) (2022) 4440–4469, https://doi.org/10.1039/D2EE01818G.

[9] E.W. Lees, J.C. Bui, O. Romiluyi, A.T. Bell, A.Z. Weber, Exploring CO_2 reduction and crossover in membrane electrode assemblies, Nat. Chem. Eng. 1 (5) (2024) 340–353, https://doi.org/10.1038/s44286-024-00062-0.

[10] A. El-Kharouf, T.J. Mason, D.J. Brett, B.G. Pollet, Ex-situ characterisation of gas diffusion layers for proton exchange membrane fuel cells, J. Power Sources 218 (2012) 393–404, https://doi.org/10.1016/j.jpowsour.2012.06.099.

[11] F.C. Cetinbas, R.K. Ahluwalia, N. Kariuki, V. De Andrade, D. Fongalland, L. Smith, J. Sharman, P. Ferreira, S. Rasouli, D.J. Myers, Hybrid approach combining multiple characterization techniques and simulations for microstructural analysis of proton exchange membrane fuel cell electrodes, J. Power Sources 344 (2017) 62–73, https://doi.org/10.1016/j.jpowsour.2017.01.104.

[12] K.U. Hansen, L.H. Cherniack, F. Jiao, Voltage loss diagnosis in CO_2 electrolyzers using five-electrode technique, ACS Energy Lett. 7 (12) (2022) 4504–4511, https://doi.org/10.1021/acsenergylett.2c02096.

[13] I.V. Zenyuk, E. Medici, J. Allen, A.Z. Weber, Coupling continuum and pore-network models for polymer-electrolyte fuel cells, Int. J. Hydrogen Energy 40 (46) (2015) 16831–16845, https://doi.org/10.1016/j.ijhydene.2015.08.009.

[14] M.R. Gerhardt, L.M. Pant, A.Z. Weber, Along-the-channel impacts of water management and carbon-dioxide contamination in hydroxide-exchange-membrane fuel cells: a modeling study, J. Electrochem. Soc. 166 (7) (2019) F3180–F3192.

[15] K.N. Grew, W.K. Chiu, A dusty fluid model for predicting hydroxyl anion conductivity in alkaline anion exchange membranes, J. Electrochem. Soc. 157 (3) (2010) B327, https://doi.org/10.1149/1.3273200.

[16] K.N. Grew, X. Ren, D. Chu, Effects of temperature and carbon dioxide on anion exchange membrane conductivity, Electrochem. Solid St. 14 (12) (2011) B127, https://doi.org/10.1149/2.011112esl.

[17] E.N. Fuller, P.D. Schettler, J.C. Giddings, New method for prediction of binary gas-phase diffusion coefficients, Ind. Eng. Chem. 58 (5) (1966) 18–27, https://doi.org/10.1021/ie50677a007.

[18] A.Z. Weber, J. Newman, Transport in polymer-electrolyte membranes: I. Physical model, J. Electrochem. Soc. 150 (7) (2003) A1008, https://doi.org/10.1149/1.1580822.

[19] A.Z. Weber, J. Newman, Transport in polymer-electrolyte membranes: II. Mathematical model, J. Electrochem. Soc. 151 (2) (2004) A311, https://doi.org/10.1149/1.1639157.

[20] A.Z. Weber, J. Newman, Transport in polymer-electrolyte membranes: III. Model validation in a simple fuel-cell model, J. Electrochem. Soc. 151 (2) (2004) A326, https://doi.org/10.1149/1.1639158.

[21] J.-W. Hurkmans, H.M. Pelzer, T. Burdyny, J. Peeters, D.A. Vermaas, Heating dictates the scalability of CO_2 electrolyzer types, EES Catalysis (2025), https://doi.org/10.1039/D4EY00190G.

[22] Z. Liu, H. Yang, R. Kutz, R.I. Masel, CO_2 electrolysis to CO and O_2 at high selectivity, stability and efficiency using sustainion membranes, J. Electrochem. Soc. 165 (15) (2018) J3371, https://doi.org/10.1149/2.0501815jes.

[23] B. Endrődi, E. Kecsenovity, A. Samu, T. Halmágyi, S. Rojas-Carbonell, L. Wang, Y. Yan, C. Janáky, High carbonate ion conductance of a robust PiperION membrane allows industrial current density and conversion in a zero-gap carbon dioxide electrolyzer cell, Energ. Environ. Sci. 13 (11) (2020) 4098–4105, https://doi.org/10.1039/D0EE02589E.

[24] S. Weisenberger, d.A. Schumpe, Estimation of gas solubilities in salt solutions at temperatures from 273 K to 363 K, AIChE J. 42 (1) (1996) 298–300, https://doi.org/10.1002/aic.690420130.

[25] C. Kim, J.C. Bui, X. Luo, J.K. Cooper, A. Kusoglu, A.Z. Weber, A.T. Bell, Tailored catalyst microenvironments for CO_2 electroreduction to multicarbon products on copper using bilayer ionomer coatings, Nat. Energy 6 (11) (2021) 1026–1034, https://doi.org/10.1038/s41560-021-00920-8.

[26] A.B. Moss, S. Garg, M. Mirolo, C.A.G. Rodriguez, R. Ilvonen, I. Chorkendorff, J. Drnec, B. Seger, In operando investigations of oscillatory water and carbonate effects in MEA-based CO_2 electrolysis devices, Joule 7 (2) (2023) 350–365, https://doi.org/10.1016/j.joule.2023.01.013.

[27] I.V. Zenyuk, P.K. Das, A.Z. Weber, Understanding impacts of catalyst-layer thickness on fuel-cell performance via mathematical modeling, J. Electrochem. Soc. 163 (7) (2016) F691, https://doi.org/10.1149/2.1161607jes.

[28] D.G. Wheeler, B.A. Mowbray, A. Reyes, F. Habibzadeh, J. He, C.P. Berlinguette, Quantification of water transport in a CO_2 electrolyzer, Energ. Environ. Sci. 13 (12) (2020) 5126–5134, https://doi.org/10.1039/D0EE02219E.

[29] A. Reyes, R.P. Jansonius, B.A. Mowbray, Y. Cao, D.G. Wheeler, J. Chau, D. J. Dvorak, C.P. Berlinguette, Managing hydration at the cathode enables efficient CO_2 electrolysis at commercially relevant current densities, ACS Energy Lett. 5 (5) (2020) 1612–1618, https://doi.org/10.1021/acsenergylett.0c00637.

[30] J. Disch, L. Bohn, S. Koch, M. Schulz, Y. Han, A. Tengattini, L. Helfen, M. Breitwieser, S. Vierrath, High-resolution neutron imaging of salt precipitation and water transport in zero-gap CO_2 electrolysis, Nat. Commun. 13 (1) (2022) 6099, https://doi.org/10.1038/s41467-022-33694-y.
[31] A.Z. Weber, R.L. Borup, R.M. Darling, P.K. Das, T.J. Dursch, W. Gu, D. Harvey, A. Kusoglu, S. Litster, M.M. Mench, A critical review of modeling transport phenomena in polymer-electrolyte fuel cells, J. Electrochem. Soc. 161 (12) (2014) F1254, https://doi.org/10.1149/2.0751412jes.
[32] J. Peng, A.L. Roy, S.G. Greenbaum, T.A. Zawodzinski, Effect of CO_2 absorption on ion and water mobility in an anion exchange membrane, J. Power Sources 380 (2018) 64–75, https://doi.org/10.1016/j.jpowsour.2018.01.071.
[33] Y. Li, T. Zhao, W. Yang, Measurements of water uptake and transport properties in anion-exchange membranes, Int. J. Hydrogen Energy 35 (11) (2010) 5656–5665.
[34] X. Luo, A. Wright, T. Weissbach, S. Holdcroft, Water permeation through anion exchange membranes, J. Power Sources 375 (2018) 442–451, https://doi.org/10.1016/j.jpowsour.2017.05.030.
[35] F. Wei, A. Kosakian, J. Liu, J. Kracher, R. Khan, M. Secanell, Water transport in anion and proton exchange membranes, J. Power Sources 557 (2023) 232494, https://doi.org/10.1016/j.jpowsour.2022.232494.
[36] J.G. Petrovick, D.I. Kushner, P. Goyal, A. Kusoglu, C.J. Radke, A.Z. Weber, Electrochemical measurement of water transport numbers in anion-exchange membranes, J. Electrochem. Soc. 170 (11) (2023) 114519, https://doi.org/10.1149/1945-7111/ad09f9.
[37] G.S. Hwang, D.Y. Parkinson, A. Kusoglu, A.A. MacDowell, A.Z. Weber, Understanding water uptake and transport in nafion using X-ray microtomography, ACS Macro Lett. 2 (4) (2013) 288–291, https://doi.org/10.1021/mz300651a.
[38] J. Biemolt, J. Singh, G. Prats Vergel, H.M. Pelzer, T. Burdyny, Preventing salt formation in zero-gap CO_2 electrolyzers by quantifying cation accumulation, ACS Energy Lett. 10 (2) (2025) 807–814, https://doi.org/10.1021/acsenergylett.4c03242.